First Limit from a Surface Run of a 10 Liter Dark Matter Time Projection Chamber

by

Thomas S. Caldwell Jr.

Submitted to the Department of Physics in partial fulfillment of the Requirements for the Degree of

Bachelor of Science

at the

Massachusetts Institute of Technology

[JUNE]

May 2009

Signature of Author _____

Department of Physics
May 8, 2009

Certified by _____

Professor Peter Fisher
Thesis Supervisor, Department of Physics

_____

Dr. Jocelyn Monroe
Thesis Co-Supervisor, Department of Physics

Accepted By _____

Professor David E. Pritchard
Senior Thesis Coordinator, Department of Physics

First Limit from a Surface Run of a 10 Liter Dark Matter Time Projection Chamber

Thomas Caldwell

May 8, 2009

Abstract

A 10 liter prototype Dark Matter Time Projection Chamber (DMTPC) is operated on the surface of the earth at 75 Torr using carbon-tetrafluoride (CF_4) as a target material to obtain a 24.57 gram-day exposure. A limit is set on a likely dark matter candidate, the weakly interacting massive particle. This is the first limit from the DMTPC detector, and the goal is to understand the sensitivity of the detector. In addition, this detector is used to measure the mean energy and attenuation coefficient of electrons propagating in CF_4.

1 Introduction

The first hint of dark matter came from measurements of galaxy cluster velocities. Prior to the 1930s, astronomers typically inferred the mass of galaxy clusters from their luminosities and internal rotations. However, this assumes that all the matter present in the cluster is luminous matter. To eliminate this assumption in the inference of cluster masses, Fritz Zwicky developed several methods to directly infer the mass from gravitational effects alone [ ]. Zwicky suggested that the velocity of galaxies near the edges of clusters could be used together with the virial theorem to determine the mass of a cluster. Zwicky applied the virial theorem to the Coma cluster and found that the mass determined from the luminosity was many times smaller than the mass inferred from the virial theorem. This discrepancy between the rotational speed of galaxy clusters and their visible mass led to the speculation that gravitating mass, which is not visible because it is not coupled to the electromagnetic

interaction, must exist in order to account for the orbital velocities of galaxy clusters. Zwicky referred to matter of this type as dark matter.

Since the 1930s, Zwicky's methods have been applied to many galaxy clusters with consistent results [ ]-[ ]. Additional methods have also found evidence for dark matter through the observation of gravitational lensing [ ]. Studies of the cosmic microwave background imply that ordinary matter could not have produced the small density fluctuations required for the observed clustering of matter into small scale structures [ ]. Dark matter solves this problem because it is not coupled to photons, and it would allow for small density fluctuations to evolve over long time scales. With solid evidence for the existence of dark matter, with an energy density of 23% of the total energy density of the universe, the focus has shifted to determining the nature of dark matter.

Based on models of structure formation, dark matter is expected to be non-relativistic so that it could sustain small density fluctuations in the early universe. Also, dark matter must be stable since we have observed its influence in the early universe along with its current influence on galactic rotation. The fact that the evidence for dark matter comes solely from its gravitational influence favors a dark matter candidate which has an extraordinarily small cross section with normal matter and with itself. Thus, the favored dark matter candidates are a class of particles known as cold collisionless dark matter (CCDM). Numerical simulations of structure formation with CCDM provide relatively good agreement with observations. Of the possible CCDM candidates, weakly interacting massive particles (WIMPs) are preferred for several reasons. First, simulations of structure formation with WIMPs can be tuned such that a total energy density of 20-30% for dark matter can be achieved, consistent with the observed 23%. Additionally, theories of supersymmetry predict a stable weakly interacting particle with mass on the order of 100 GeV known as the neutralino [ ]. Furthermore, WIMPs in thermal equilibrium in the early universe would have undergone thermal freeze out, resulting in a relic dark matter abundance inversely proportional to the interaction cross section. Since WIMPs are only weakly interacting, their interaction cross section must be on the weak scale, so a particle with mass on the order of the neutralino's predicted mass would give a relic dark matter density that is consistent with observations. So, supersymmetric theories provide a natural WIMP candidate.

Although WIMPs as a form of CCDM are the candidate for dark matter, several other possibilities exist. One appealing candidate is the axion which would play an

important role in explaining the lack of large CP violation in strong interactions [8][9]. The axion would be a neutral particle with mass on the order of 1 μeV, and would have a very weak coupling with electromagnetism. Several experiments are under way which search for the decay of an axion into two photons in an intense magnetic field [10]. Several alternatives to CCDM (strongly self-interacting dark matter, warm dark matter, repulsive dark matter, self-annihilating dark matter, etc.) have been constructed in attempts to accommodate the possible small scale discrepancies of CCDM halo distributions with observations and simulations [11]. However, CCDM, and WIMPs in particular, have remained the favored candidate for dark matter. This is the type of dark matter sought by the DMTPC collaboration.

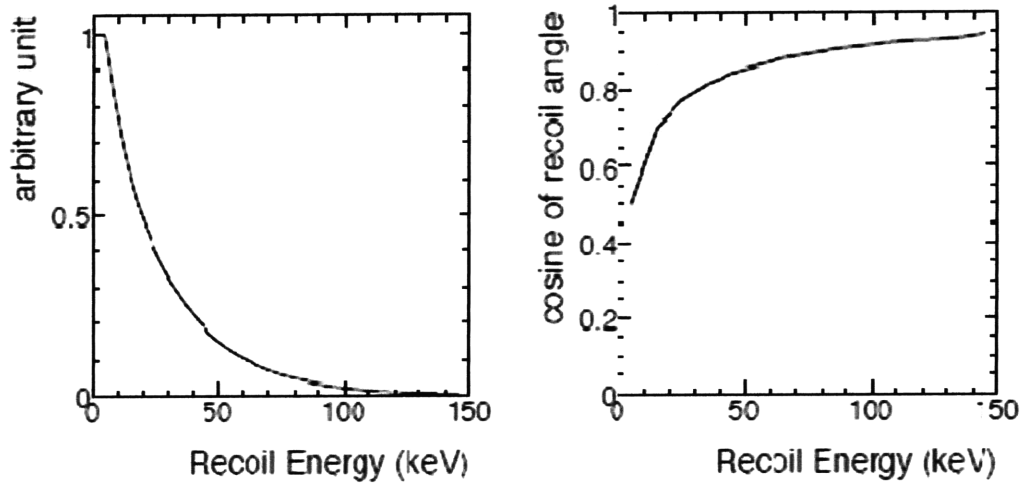

Figure 1: Figure 1. Energy spectrum and distribution of the cosine of the recoil angle versus recoil energy for fluorine recoils induced by 100 GeV WIMPs in CF_4.

1.1 WIMP Detection Possibilities

Many experiments attempting to detect WIMPs are underway, and the majority of such experiments focus on the direct detection of WIMPs. All direct detection dark matter experiments search for the interaction of a dark matter particle with a nucleus of the detector material. Since WIMPs interact only weakly and gravitationally, the sought signal is a recoiling nucleus within the detector material, so direct detection

experiments must be able to identify a low energy recoiling nucleus. For a gaseous CF_4 detector, as will be used in the measurements presented here, the expected energy distribution for 100 GeV WIMP induced recoiling fluorine nuclei is primarily below 50 keV, as shown in Figure 1. The detection of low rate nuclear recoils at these low energies is the primary challenge to WIMP direct detection.

Most direct detection experiments look for this low energy nuclear recoil signal in gaseous, liquid, or solid detector volumes by looking for the scintillation and/or charge created by the interaction. This experiment and various others (DRIFT, NEWAGE) utilize gaseous detector target volumes, while other experiments utilize liquid (COUPP, XENON, PICASSO) or solid (DAMA, CDMS, CRESST, KIMS) target volumes. Gaseous detectors have the advantage that a low energy recoiling nucleus will travel a further distance before depositing all of its energy than in a liquid detector. This gives gaseous detectors a superior ability to reject backgrounds. However, gaseous detectors suffer from a much lower density of targets in the detector volume, so liquid or solid based detectors can expect a higher rate of interactions and can more easily be scaled to large target masses.

A WIMP direct detection experiment can expect to detect recoiling nuclei of mass M from WIMPs of mass m with local density ρ at a rate per unit detector mass, R, of

$$R(t) = \int_{E_1/Q}^{E_2/Q} \mathrm{d}E\epsilon(QE)\frac{\rho}{2m\mu^2}\sigma(q)\eta(E,t) \tag{1}$$

where E_1 to E_2 is the observed recoil energy range, $\mu = mM/(m+M)$ is the reduced mass, Q is the quenching factor (the ratio of the observed recoil energy to true recoil energy), $\epsilon(QE)$ is the efficiency of the recoil detection, $\sigma(q)$ is the WIMP-nucleus cross section for nuclear recoil with momentum q, and $\eta(E,t)$ is the mean inverse speed of the WIMP velocity distribution [ ]. For the purposes of comparing measurements, a WIMP mass m of 100 GeV with density ρ of 0.4 GeV/cm^3 is typically assumed, and the time-varying velocity distribution is taken from cosmological measurements of the local WIMP distribution and the earth's rotation and orbital motion. The efficiency $\epsilon(QE)$ depends on the particular experiment's signal cuts, recoil detection method, etc. The remaining piece of Equation 1 is the WIMP-nucleus total cross section σ. In general, the cross section has contributions from both spin-independent (SI) and spin-dependent (SD) couplings

$$\sigma = \sigma_{SI} + \sigma_{SD} \tag{2}$$

For a nucleus with Z protons, $A - Z$ neutrons, and nuclear form factor $F(E)$, the SI

contribution to the total WIMP-nucleus cross section is given by

$$\sigma_{SI} = \frac{4\mu^2}{\pi} [Zf_p + (A - Z)f_n]^2 |F(E)|^2 \quad (3)$$

where f_p and f_n are WIMP couplings to the proton and neutron respectively. The contribution due to SD couplings for a nucleus with spin J and momentum exchange dependent structure functions $S_{pp}(q)$, $S_{nn}(q)$, and $S_{pn}(q)$ is given by

$$\sigma_{SD} = \frac{32\mu^2 G_F^2}{2J+1} [a_p^2 S_{pp}(q) + a_p a_n S_{pn}(q) + a_n^2 S_{nn}(q)] \quad (4)$$

where G_F is the Fermi coupling constant and a_p and a_n are the axial four-momentum WIMP-nucleon couplings in units of $2\sqrt{2}G_F$. Comparing Equations 3 and 4, it is clear that SI interactions will benefit from the A^2 dependence of the cross section, while the SD contribution will not. However, SD interactions are predicted to dominate SI interactions in models where there is a substantial Higgsino contribution to the lightest super-symmetric particle [ ][ ]. In this experiment, we utilize the strong S_{pp} coupling of ^{19}F ($J = 1/2$) in the form of CF_4 to make SD measurements.

Although most experiments focus on the direct detection of WIMPs, some experiments attempt to observe the signature of WIMPs interacting with bodies more massive than any possible direct detection apparatus [ ]. For example, some experiments look for the high energy neutrino signatures from WIMP capture by the sun. Other experiments look for particle signatures of WIMP capture and annihilation in the galactic center or in the earth itself.

1.2 Directional Detection

Simple models of our Galaxy's WIMP distribution predict that a WIMP wind of speed 220 km/s should pass through the earth due to the sun's orbital motion around the galactic center. The earth's rotation axis is oriented approximately 48 degrees from the direction of this anticipated WIMP wind, so in 12 hours the direction of the WIMP wind relative to an observer on the surface of the earth should change by approximately 90 degrees [ ]. Direct detection of a WIMP signal which is consistent with this direction time variation would provide unambiguous evidence for the detection of dark matter.

The primary advantage to using gaseous detector volumes for the direct detection of WIMPs is that at low pressures (<100 Torr), recoiling nuclei will travel a few millimeters before depositing all of their energy. So, with 3-dimensional track

reconstruction and spatial resolution on the order of a few hundred microns, one can determine the 3-dimensional angle at which the recoiling nucleus traveled. Figure 1 shows the expected angular distribution of fluorine nuclear recoils from 100 GeV WIMPs, and as can be seen from the figure, the recoil angle encodes the direction of the incident WIMP even down to 10s of keV. In addition to the ability of low pressure gaseous detectors to measure the track angle of a nuclear recoil, examination of the track's energy distribution can provide the direction that the recoiling nucleus traveled along that axis [ ]. This is known as the head-tail effect since the stopping power peaks at low energy, and so measuring the energy loss along the track provides information about the vector direction, or 'head' vs. 'tail' of the track (see Figure 5). Therefore, low pressure gaseous detectors capable of precise 3-dimensional track reconstruction may have the ability to demonstrate the time varying WIMP signal which would provide unambiguous evidence for the detection of dark matter. In addition, detectors capable of making such measurements may be able to provide means to study local dark matter distributions [ ][ ].

2 Experimental Apparatus and Data Acquisition

The DMTPC detector is a directional dark matter detector designed with the goal of measuring the direction and energy of nuclear recoils caused by incident WIMPs. The detector is a low pressure time projection chamber which utilizes low pressure (75 Torr) CF_4 gas as a target material such that recoiling nuclei from dark matter interactions would travel a few millimeters. CF_4 has an average ionization energy of about 54 eV, so nuclear recoil interactions produce on the order of 10^3 primary electrons which drift towards an amplification region. Electrons which reach the high electric field of the amplification region are multiplied by avalanche multiplication which also produces scintillation photons. The process is optically read out by a CCD camera giving a two-dimensional profile of the track. The tracks are then reconstructed to determine the energy of the interaction, and the track profile is used to determine the two-dimensional direction of the incident particle.

A schematic of the Dark Matter Time Projection Chamber (DMTPC) detector used in this experiment is shown in Figure 2. A 75 liter stainless steel vacuum vessel manufactured by Kurt Lesker contains two identical back-to-back time projection chambers, one of which is shown in Figure 2. Each time projection chamber contains a wire cathode mesh and a grounded anode mesh separated by 19.7 cm. The meshes

are composed of 28 μm stainless steel wire with a pitch of 256 μm. The meshes are stretched to high tension and fixed to a circular stainless steel ring with inner diameter of 27 cm. The grounded anode mesh is separated from a solid copper anode plate by fluorocarbon wires with a diameter of 500 μm, in order to create a high electric field in the amplification region. The fluorocarbon wires are placed at 2.0 ± 0.1 cm intervals in order to maintain even spacing between the mesh and anode plate. The two time projection chambers are separated by a layer of G10 to electrically isolate the two amplification regions.

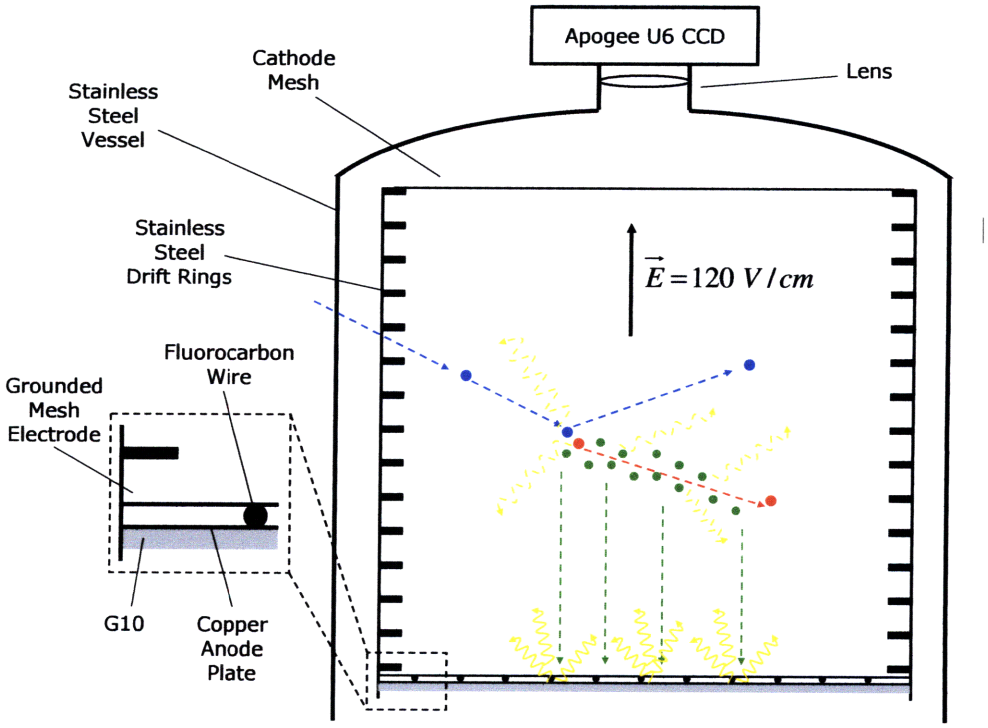

Figure 2: A schematic of the DMTPC detector. Also shown is a particle (blue) interacting with a CF_4 molecule in the detector. The recoiling nucleus (red) produces primary scintillation (dashed yellow) and electrons (green) which drift towards the amplification region. The avalanche charge multiplication then produces scintillation (yellow) which is recorded by the CCD camera.

Each time projection chamber also contains a drift cage to ensure uniform electric field in the direction perpendicular to the plane of the meshes. The drift cages consist of a series of 27 cm inner diameter and 32 cm outer diameter stainless steel rings with

thickness 1 mm connected by 1 MΩ resistors. The rings are then separated by 1 cm using nylon washers. The size and separation of the rings was optimized using finite element calculations to minimize the variation in electric field and to minimize the amount of material introduced into the detector. An electric field component parallel to the wire meshes of less than 1% is achieved in the entire fiducial volume, the region of the detector's active target mass, according to finite element simulations.

The detector's primary form of readout is the two-dimensional optical readout of scintillation photons created in the avalanche charge multiplication process. This scintillation light is collected with a Nikon photographic lens with f-stop ratio of 1.2 and a focal length of 55 mm. The scintillation light is recorded by an Apogee U6 camera with a Kodak 1001E CCD chip. The camera contains 1024 × 1024 channels, however, the data taken in this experiment utilized a camera intrinsic 4 × 4 binning in order to optimize the signal to noise ratio and decrease the chip readout time. Each pixel in the CCD images 143 μm × 143 μm of the anode plane, so the 4 × 4 binning results in bins which image 572 μ × 572 μm of the anode plane. The camera images a total of 14.64 cm × 14.64 cm, so the fiducial volume for each time projection chamber is 4.22 liters. In addition to the optical readout, the charge deposited on the anode is also read out by an oscilloscope which is connected to the copper anode plate. However, this charge information was not used in taking the data presented here.

The vacuum vessel containing the time projection chambers is filled with low pressure CF_4 gas, typically 75 Torr. At this pressure a typical recoiling carbon or fluorine nucleus would travel 1-2 mm before depositing all of its energy. CF_4 is chosen as a target material due to its high fluorine content. ^{19}F is a particularly good target material for spin-dependent measurements due its large spin factor and isotopic abundance [ ][ ]. Also, CF_4 produces about 1 scintillation photon in the 200-800 nm wavelength region for every 3 avalanche electrons [ ], so CF_4 provides good scintillation light in the wavelength region where the quantum efficiency of the CCD is highest. CF_4 also has good electron diffusion characteristics, allowing drift distances of 25 cm before the electron transverse diffusion is on the order of millimeters.

Prior to the start of acquiring data, the vacuum vessel is evacuated to approximately 10 mTorr and is pumped on in this state for approximately 24 hours in order to reduce the rate of outgassing. To obtain the data presented here, the chamber was then filled with CF_4 at a pressure of 75 ± 1 Torr, and voltages of -3.0 kV and +0.68

kV were applied at the cathode mesh and anode plane respectively. Prior to acquiring each 3000 event subset of data, 100 dark frames, images taken with the camera shutter closed, are averaged by the camera and then saved to be used as a bias frame. The bias frame is used to correct for pixel-to-pixel variations in the analysis of the data. The camera is operated by taking a 1 second exposure, then closing the shutter, and then readout of the exposure. The readout time of the camera is on the order 100 ms. Data was acquired in sets of 3000 exposures before saving and transferring the data. The data acquisition cycle was approximately 24 hours and consisted of 15 consecutive 3000 exposure runs followed by the evacuation of the chamber down to approximately 10 mTorr and a refill of the chamber back to 75 Torr. This was done in order to maintain a consistent gas gain over the course of data taking. Electronegative contaminants in the gas due to leaking or outgassing can drastically reduce the number of electrons which reach the amplification region. Prior to acquiring data, the gain stability was measured using the reconstructed energy of tracks from an ^{241}Am alpha source which emits alphas primarily at energies 5.486 MeV (86%), 5.443 Mev (12.7%), and 5.391 MeV (1.4 %). We found that the gain was stable to approximately 1% over 24 hours. Therefore, evacuating and refilling the chamber every 24 hours ensured that the gain was stable to 1%. This results in an uncertainty of the same order of magnitude as the uncertainty on the pressure measurement which arises from 1 Torr pressure sensitivity of the Inficon PCG400 pressure gauge which utilizes a combination of a capacitance and a Pirani gauge.

At 75 Torr of CF4 with the 14.64 cm $\times$ 14.64 cm view field and the 19.7 cm drift region, the active fiducial mass is 1.49 gm, since only one time projection chamber was active during the data taking. 458 runs each containing 3000 exposures were acquired in the WIMP search data run, giving 15.90 days of live time. Therefore, the total exposure was 23.69 gm-days. In addition, to calibrate the detector and better understand backgrounds, separate smaller data sets were acquired, some with an ^{241}Am alpha source and some with a ^{252}Cf neutron source. Data was also taken with the camera shutter closed in order to understand backgrounds which may arise from the interaction of particles with the CCD chip itself, and a similar set of data was taken with the CCD camera inside a 20 cm thick cube of borated polyethylene to reduce the CCD backgrounds from cosmic ray neutrons.

3 Analysis of Data

3.1 Length and Energy Calibration

Figure 3 shows an example of the data used in the length and energy calibrations of the detector. Four collimated ^{241}Am alpha source were placed in the CCD camera's view field; these are fixed to rods which are attached to the rings of the drift cage at different heights. For the purposes of the length and energy calibrations, only the source on the far right of the image is used, since it was placed at the smallest drift distance. The length calibration will rely on observing gaps in tracks caused by the fluorocarbon wire spacers which separate the ground mesh from the anode plate. These wires are placed at 2.0±0.1 cm, so by relating this distance to a number of pixels in CCD images, we can determine how much area each pixel images on the anode plane.

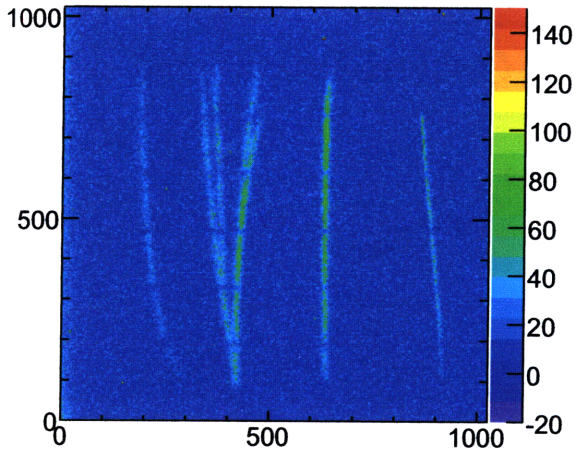

Figure 3: An example of the data used for the detector's length and energy calibration. Four ^{241}Am alpha sources are attached at different drift distances to the drift cage. The gaps seen in the tracks are the result of the fluorocarbon wire spacers. Both axes are in units of CCD pixel number.

To identify the location of the wire spacers, we sum a large number of images from the WIMP search. By projecting onto the vertical axis, it was determined that 140±2 pixels correspond to the vertical distance between spacers. Figure 4 shows

the result of this procedure, and the dips in the histogram correspond to the location of the spacers. In order to relate this value to the 2 cm separation of the spacers, we also need to determine the angle at which the spacers lie in the plane. Using the histogram shown in Figure 4, this angle was determined to be 3.6 degrees with respect to the horizontal axis. Using these values, we then determine that each pixel images a 143±7 μm square region in of the anode plane.

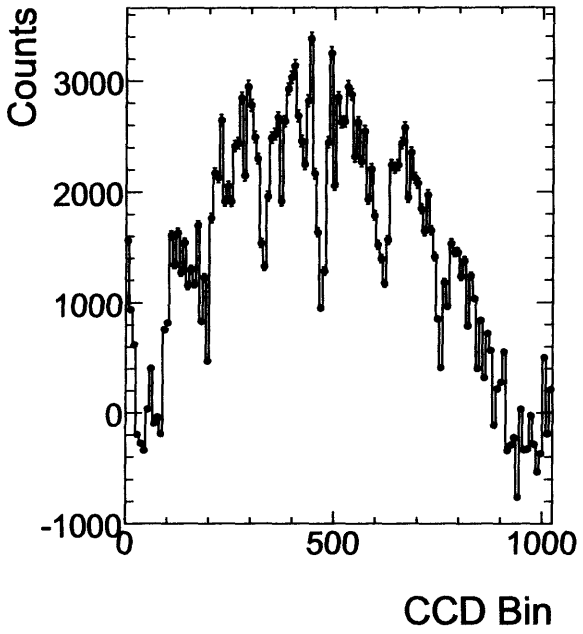

Figure 4: The projection of 50 alpha tracks onto the vertical axis of Figure 3. The dips in the distribution correspond to successive fluorocarbon wire spacers.

With this same calibration data, we can compare the track profile of alpha particles from the ^{241}Am source to the SRIM Monte Carlo prediction. Again, the source with the smallest drift distance was used. The energy of this source was independently calibrated using a solid state detector and multichannel analyzer. Although ^{241}Am emits primarily 5.486 MeV alpha particles, the measured alpha source has a primary peak at 4.295 ± 0.023 MeV, due to likely energy loss in a small window in front of the source. Figure 5 shows the SRIM prediction for the stopping power of a 4.295 MeV alpha particle in 75 Torr of CF_4. Using 6000 images similar to the one shown in Figure 3, we compare track profile segments in the calibration data to the

curve in Figure 5 by projecting segments which do not cross spacers onto the vertical axis, integrating the resulting distribution, and comparing this integral to the same integral for the SRIM prediction. The ratio of the measured yield, in ADC counts, to the predicted integral gives the energy calibration constant.

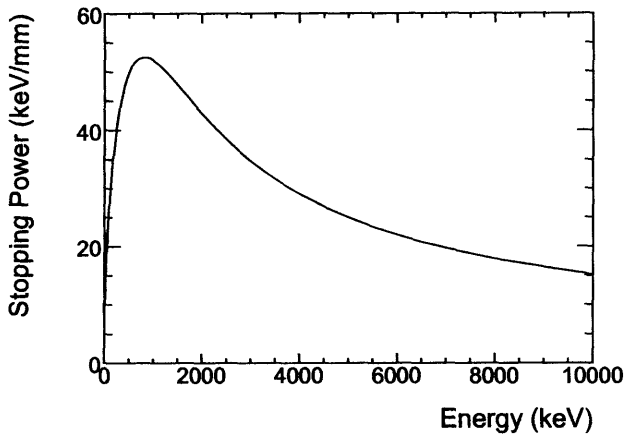

Figure 5: The stopping power versus energy of an alpha particle in 75 Torr of CF_4.

Since we project onto the vertical axis, we must first select tracks which are parallel to this axis in order to compare with the SRIM prediction. This is done by projecting the track onto the horizontal axis, fitting to a gaussian distribution, and selecting only those tracks with spread less than 10 bins. After selecting the appropriate tracks, nine 5.72 mm long segments are chosen along the track such that the fluorocarbon wire spacers are avoided. These segments are projected onto the vertical axis and integrated to obtain the number of counts in that region of energy loss (see Figure 6). Comparing the mean over all selected events of the integral from each segment to the appropriate integral of the SRIM prediction curve in Figure 5, we obtain a number of counts per keV of energy loss in each segment. Taking the mean of these values, we determine an energy calibration of 3.46±0.11 counts/keV.

3.2 Track Reconstruction

The raw CCD images are first background subtracted using the dark frame, an average of 100 frames taken with the camera shutter closed, saved at the beginning of each 3000 event run. This removes the large pedestal in the data and the position dependence of the CCD noise background. After this background subtraction, the mean

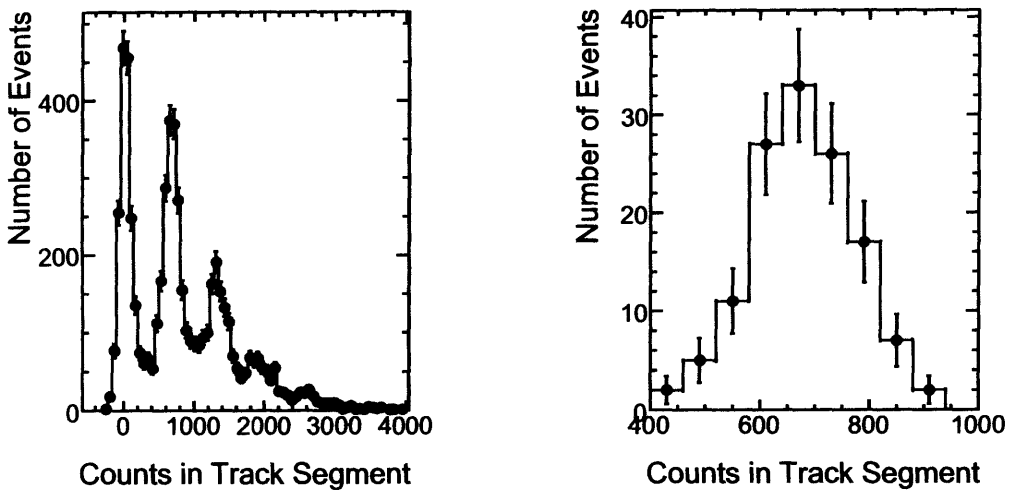

Figure 6: Left: The integral of the number of counts over a 5.72 mm region starting 22.9 mm from the source for all events; successive peaks are from multiple track events. Right: The integral of the number of counts over the same region for the selected events which contain a single track parallel to the image's vertical axis.

of empty frames still varies with time due to effects in the CCD, likely related to the temperature of the readout electronics. To correct for this, the image is then further background subtracted by centering the distribution of counts from non-outlier pixels, selected using an iterative procedure, to zero. Effectively, this uses pixels which are not part of tracks in order to center the noise distribution of each frame to zero. On average, the resulting images have an RMS noise level of approximately 6.5 counts. Prior to scanning for tracks, the image is scanned for pixels which are systematically many times the noise RMS above background. These pixels are excluded from the image; typically $\sim$5 such pixels are found per frame.

After these data cleaning steps, the data images are then scanned in software for tracks. To aid in the identification of tracks, a copy of the image is first rebinned and blurred. The camera saves the data in 4 by 4 pixel bins, and for the purpose of track identification, the image is rebinned into bins which correspond to 8 by 8 pixels. The image is blurred by setting each bin to its value plus a weighted average of the neighboring bins. Blurring the image helps in track identification because it reduces the noise variations within the track and speeds up the track identification process. After these steps, the data is then scanned for tracks. A track is identified

if a group of 5 adjacent pixels is found to be 3σ above background. The tracks found are then mapped back to the images which have not been rebinned and blurred. Then, tracks which lie within 3 bins of each other are joined into a single track under the assumption that the gap is the result of the track crossing a spacer wire. 15000 images were visually scanned and compared to the track finding algorithms to verify that tracks were correctly identified and that tracks crossing spacers were correctly joined. Given the thresholds for track identification that the noise level of the images is on average 6.5 counts, we expect a threshold of approximately 10 keV per blurred bin, or 11.4 keV/mm. With the requirement that 5 contiguous pixels be above threshold to constitute a track, this corresponds to an energy threshold of approximately 50 keV for track recognition. In addition, the threshold of 11.4 keV/mm has the consequence that the detector is blind to the Compton scattering of electrons which are minimum ionizing particles having a stopping power of only 0.08 keV/mm, far below the detector's threshold.

After all tracks have been identified, the vertex, projected energy, projected range, recoil angle, and skewness are then reconstructed for each track. The energy of the recoil is reconstructed simply by integrating the counts for all pixels in track and then dividing by the energy calibration of 3.46 counts/keV, and this corresponds to the energy transferred to a recoiling nucleus through an interaction in the detector volume (or in the case of alpha particles, the energy of the emitted alpha). The projected range is determined by finding the maximum distance between any two pixels in the track, and this corresponds to the distance projected onto the 2-dimensional image plane between the location of an interaction and the end of the particle's energy loss. The recoil angle is defined as the angle in the plane of the image with respect to the horizontal axis, in the CCD frame, between the two pixels of maximum separation in the track. This corresponds to the direction of the recoiling particle and is correlated with the direction of the incoming particle, as shown in Figure 1. The skewness (the third standardized moment about the mean) is calculated along the axis defined by the reconstructed angle. The skewness can is used with the head-tail effect to measure the vector direction of the recoil (see Figure 5).

3.3 Measurement of Electron Diffusion Characteristics in CF_4

The DMTPC detection concept relies on the diffusion of electrons through low pressure gas in regions of relatively low electric field. As electrons from the primary interaction of a particle in the gas drift towards the amplification region, the electron

signal spreads both transversally and longitudinally. In addition, there is electron attachment to CF_4 molecules as electrons drift, and this reduces the signal seen in the amplification region. Precise measurements of these diffusion characteristics is vital to the design and understanding of the DMTPC detector. Although several measurements have been made of the transverse electron diffusion [ ]-[ ] and electron attachment [ ]-[ ] in CF_4, the measured values vary by up to an order of magnitude.

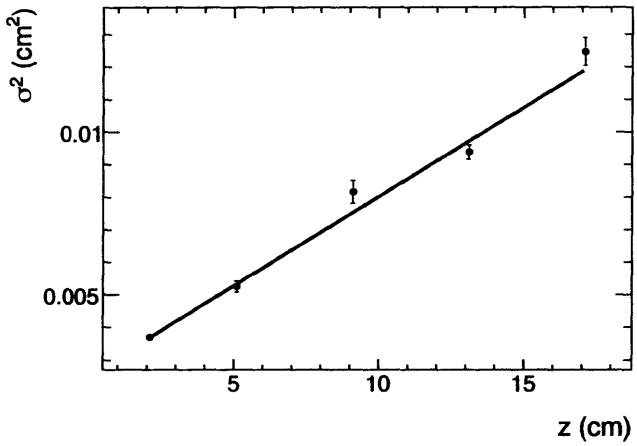

Figure 7: Fit of a linear function to σ^2 versus z for one E/N point.

Placing several ^{241}Am sources at different drift heights in the DMTPC detector, we are in a position to make relatively precise measurements of these electron diffusion characteristics. This is because the squared width, σ^2, of a track is expected to change linearly with the drift distance, z, due to electron transverse diffusion according to

$$\sigma^2 = \sigma_0^2 + 2\left(\frac{D}{\mu}\right)\left(\frac{zL}{V}\right) \tag{5}$$

where V is the applied voltage in a drift cage of length L, σ_0^2 is the intrinsic detector resolution, D is the diffusion constant, and μ is the electron mobility. So, measuring the width of tracks of known energy at varying drift heights allows for measurement of the diffusion parameter D/μ. Furthermore, comparison of the magnitude of the signal seen from the tracks at varying drift distances allows for a measurement of the attenuation of the signal due to electron attachment. A signal of initial strength I_0 will be attenuated to a strength I as a function of drift distance z according to

$$I(z) = I_0 e^{-\eta z} \tag{6}$$

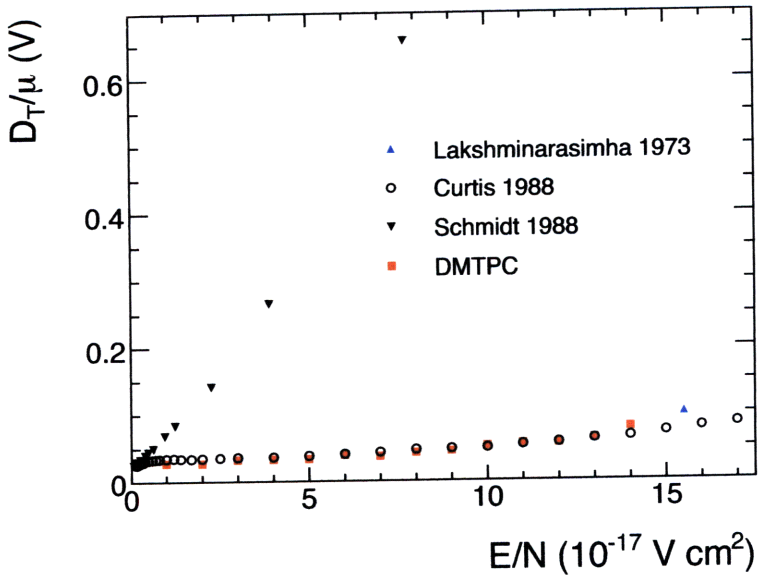

Figure 8: Measured values of D/μ as a function of E/N compared with other measurements.

where η is the attenuation coefficient.

In order to measure the diffusion, five ^{241}Am sources were attached to the rings of the drift cage at heights of 2.1 ± 0.1 cm, 5.1 ± 0.1 cm, 9.1 ± 0.1 cm, 13.1 ± 0.1 cm, and 17.1 ± 0.1 cm. A 1.2 mm long segment of the alpha tracks at a distance of 3 cm from the source is projected onto the axis perpendicular to the track for each of the sources. The resulting transverse profile is then fit to a gaussian distribution, and the square of the standard deviation of the distribution is taken to be σ^2 in Equation 5. Obtaining σ^2 values for each of the sources, a line is fit to the σ^2 distribution as a function of z in order to extract a value for D/μ. An example of the fit to Equation 6 for the data is shown in Figure 7. In order to compare results to existing measurements we measure values for D/μ as a function of the reduced electric field E/N. This is done by taking data at varying pressures (50-150 Torr) and drift voltages (1-5 kV). The results are shown in Figure 8, and the results are in agreement with the values from [24] and [25] but do not agree with the measurements from [23]. For a more detailed discussion of the measurement, see [28].

In order to measure the attenuation of a signal due to the attachment of electrons to CF_4 molecules, a setup similar to that described above is used, but an ^{55}Fe X-

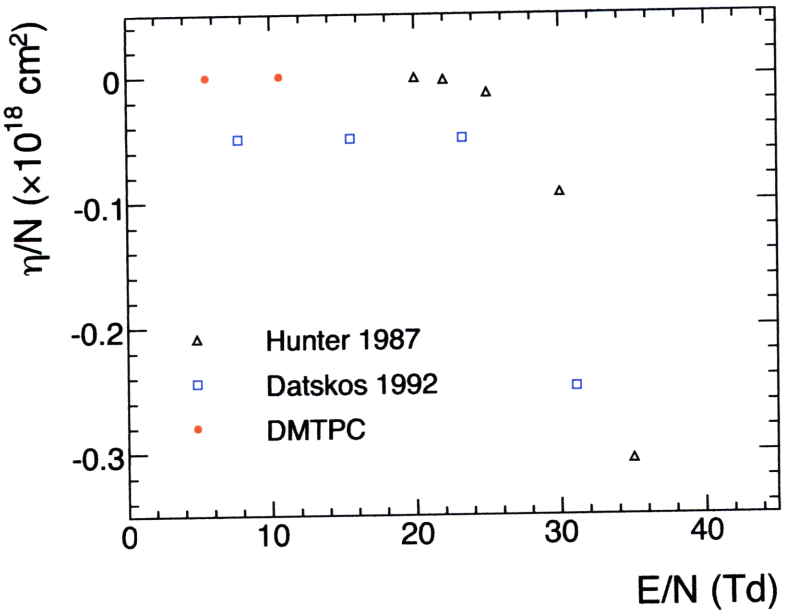

Figure 9: Reduced attenuation coefficient as a function of reduced electric field compared with previous measurements.

ray source (5.9 keV) is used rather than the ^{241}Am sources. The ^{55}Fe source is placed at varying drift heights, and the integral of the charge deposited on the anode (after subtracting a background taken with no source present) is taken to be the intensity of the signal for the particular z value. The measurements for varying values of z are fit to an exponential (Equation 6) to give the measured value for the attenuation coefficient. η is then scaled by dividing by N to allow comparison to existing measurements. This was done for two values of E/N, and the results are shown in Table 1 and in Figure 9 in comparison to existing measurements. The results show that the measured value for the attenuation coefficient η/N is consistent with zero; in agreement with [26] but in disagreement with [27].

3.4 Backgrounds to the Data

To identify nuclear recoils caused by dark matter particles interacting in the detector's fiducial volume, we must identify and reject sources of background. We identify all interactions found in the data from this surface run of the detector as backgrounds

E/N ($\times 10^{-17}$ V·cm^2)	$\eta/N \pm \sigma_{stat}$ ($\times 10^{18}$ cm^2)
5.5	-0.00026 ± 0.00006
10.6	0.00027 ± 0.0001

Table 1: Measured values of the attenuation coefficient in CF_4. Systematic errors are estimated to be less than 3%.

because dark matter scattering has been excluded by several other experiments at the level of our detector's current sensitivity. Therefore, we do not expect to see any true dark matter induced nuclear recoil signal events. These sources of background include alpha particles from decays of radon chain daughters in detector materials, camera artifacts, and ambient neutrons interacting in the gas.

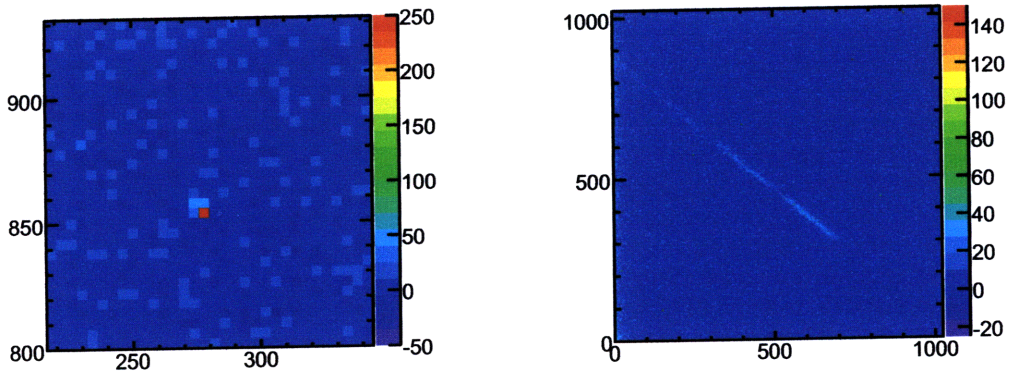

Figure 10: Left: A background worm event, characterized by a few pixels at very high energy. Right: An alpha particle coming from the side of the detector.

One source of such camera backgrounds are events in which a particle, from a gamma or cosmic ray for example, interacts directly with the CCD chip, creating a very localized region of high energy. A similar background can be caused by random fluctuations in the CCD causing a localized region of high energy. These events are referred to as worms, and an example is shown in Figure 10. In order to better understand this source of background, data was taken with the shutter of the CCD camera closed, so that worms should be the only tracks identified in the analysis. Figure 11 shows the energy distribution of the tracks identified in this set of data. Also shown in the figure is the range versus energy distribution of tracks identified and,

for comparison, the SRIM Monte Carlo predictions for recoiling carbon or fluorine nuclei. These events can be identified and cut from the data with relative ease by their high energy density as compared to a track from a nuclear recoil. As a further study of these events, the CCD camera was surrounded on all sides by 20 cm of borated polyethylene in order to reduce the neutron flux incident on the camera to a few percent. Taking data with this shielding resulted in 25% fewer worm events than in an equal amount of data without the shielding. Thus, we expect that roughly 25% of the worms found in the data are the result of cosmic ray neutrons interacting directly with the CCD chip. The remaining population of worms is expected to be caused by other particle interactions with the CCD and random fluctuations in the CCD resulting in localized regions of increased charge.

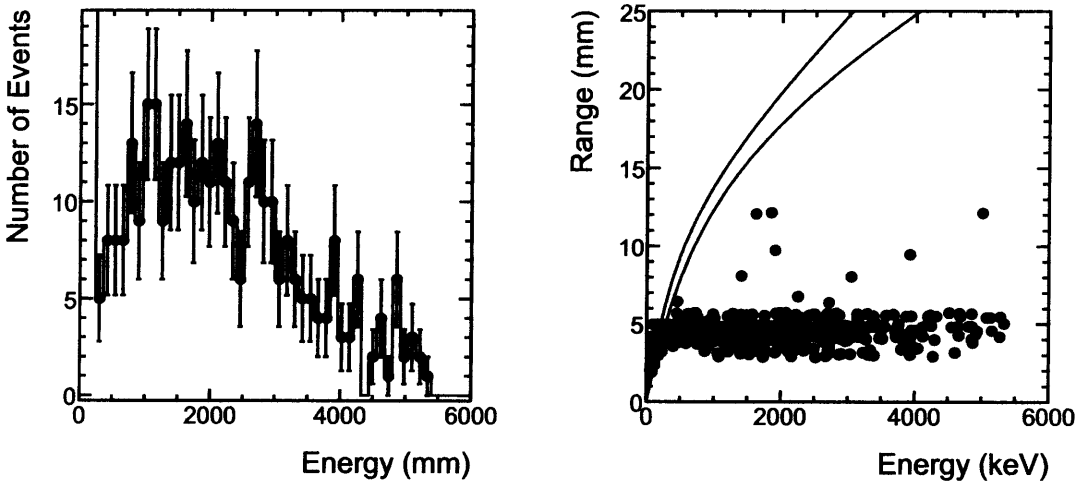

Figure 11: Left: The reconstructed energy distribution for the background data with no cuts applied. Right: The range versus energy distribution of the background data, along with the SRIM predictions for recoiling fluorine (top) or carbon (bottom) nuclei for comparison.

Another potential source of background comes from alpha particles emitted by radioactive materials within the detector. Since the majority of the material which comprises the detector is located in the drift cage and vacuum vessel, the majority of such events should be tracks that cross the edge of the camera's view field. An example of such an event is shown in Figure 10. These events can be easily identified and cut from the data since they cross the edge of the image. However, alphas emitted

by radioactive impurities in the gas or in the anodes may be contained entirely in the camera's view field. Such events can be identified and cut by their range versus energy distribution, which differs from that of nuclear recoils shown in Figure 18.

3.5 Signal Selection

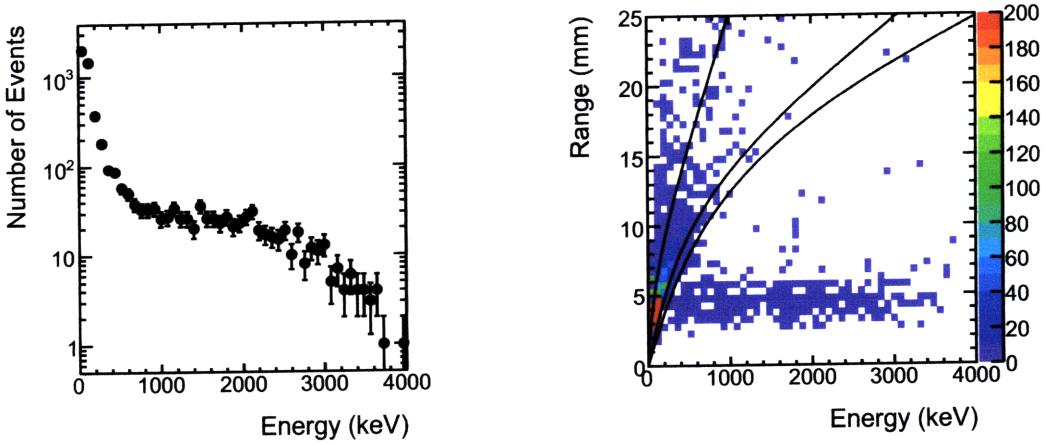

Figure 12: Energy (left) and range versus energy (right) distributions for the events in the ^{252}Cf data set which pass the cuts on sparks and multiple tracks. Also shown are the SRIM predictions for alphas (top) and recoiling F (middle) and C nuclei (bottom).

In order to understand the detector response to nuclear recoil events and to determine the signal selection cuts, the detector was placed approximately 2 meters from a ^{252}Cf neutron source with an activity of approximately 2 mCi. The energy spectrum for neutrons emitted by ^{252}Cf has a peak near 1 MeV, and the distribution then tails off to about 10 MeV [29]. Based on this distribution, we expect to see recoiling nuclei up to approximately 2 MeV in energy. The data taken with the ^{252}Cf source is analyzed with the analysis structure used to analyze the WIMP search data. The neutron data set consists of 18000 one second exposure frames. Applying the reconstruction analysis to this data set, 11261 events are found to contain tracks. An initial signal selection cut is applied which removes events in which 55000 pixels are above threshold. This eliminates tracks which are found due to electrical sparking within the chamber. Next, a cut which eliminates all events in which multiple tracks

are found is applied because the analysis framework is not currently in a stage to appropriately handle multiple track events. Applying these cuts, there are 5036 events which are not sparks and contain a single track. The energy and range versus energy distributions for the reconstructions with these cuts applied is shown in Figure 12. For comparison, all subsequent range versus energy plots show the SRIM Monte Carlo predictions for alpha particles, recoiling fluorine nuclei, and recoiling carbon nuclei all in 75 Torr of CF_4.

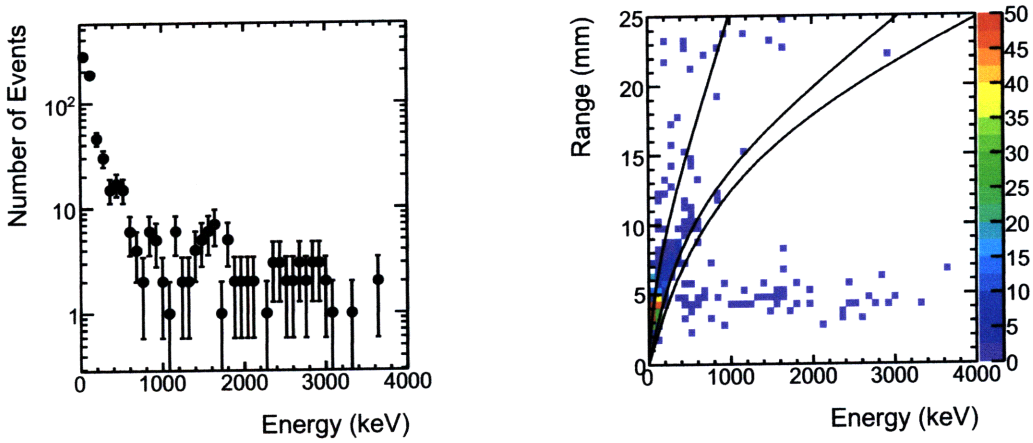

Figure 13: Energy (left) and range versus energy (right) distributions for the events in the ^{252}Cf data set which pass the cuts on sparks, multiple tracks, and worm events. Also shown are the SRIM predictions for alphas (top) and recoiling F (middle) and C nuclei (bottom).

At this stage, the distributions should contain the nuclear recoil events of interest along with backgrounds from alpha particles and worms from camera effects. Examining Figure 12, there is a population of events which is consistent with the SRIM predictions, and another population which is consistent with the worm events from Figure 11. Now, we apply a cut to eliminate worm events based on the data from Figure 11. Tracks which have an energy density greater than 36.4 keV/mm and size of less than 64 bins are tagged as worms and cut from the data, leaving 688 events. Figure 13 shows the energy and range versus energy distributions for the neutron data after application of the the worm cut. The figure shows that the cut has eliminated the majority of the events consistent with the worm events which arise from interactions with the CCD itself and other intrinsic camera effects.

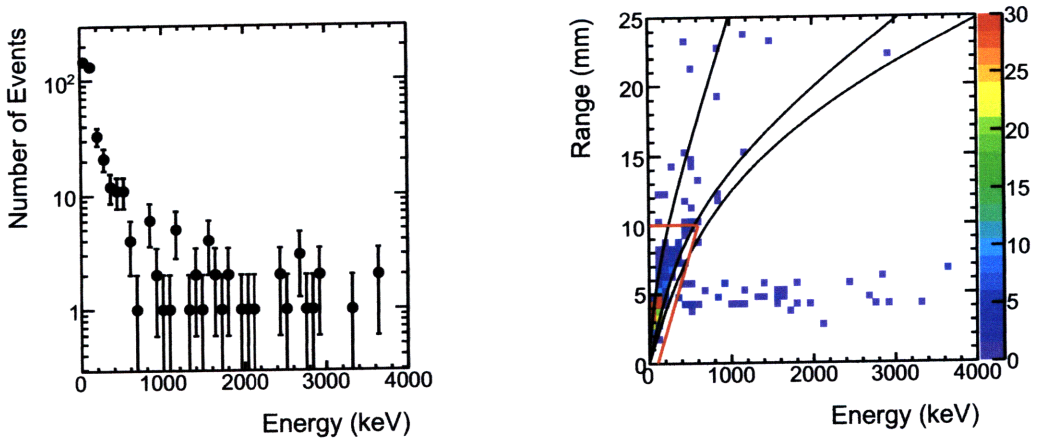

Figure 14: Energy (left) and range versus energy (right) distributions for the events in the ^{252}Cf data set which pass the cuts on sparks, multiple tracks, worms, and edge crossing events. Also shown are the SRIM predictions for alphas (top) and recoiling F (middle) and C nuclei (bottom). Shown in red is location of the cut on range versus energy which will be applied.

Although some worm events still remain in the data, the primary background at this stage is the background due to alpha particles emitted by materials in the detector. Since the majority of the detector material is in the drift cage and the vacuum vessel, the majority of these background alphas should originate from outside the view field of the camera. These events can be eliminated by a signal selection cut which eliminates events crossing the edge of the image. This is done by requiring that every pixel in a track be at least 2.29 cm away from any of the edges of the image. The value of 2.29 cm is a very conservative value for this cut, and a better efficiency may be achievable by reducing this value. Figure 14 shows the energy and range versus energy distributions for the 415 events which pass the cut on edge crossing events. As can be seen from the figure, the cut has eliminated a substantial number of the events which are consistent with the alpha particle SRIM prediction, and some of the population of lower energy events which appear to be consistent with the SRIM prediction for recoiling fluorine nuclei.

Now, we are in a position to exploit the range versus energy discrimination of the detector and apply a signal selection cut to select only events which are consistent with expected range versus energy distribution of recoiling fluorine or carbon nuclei.

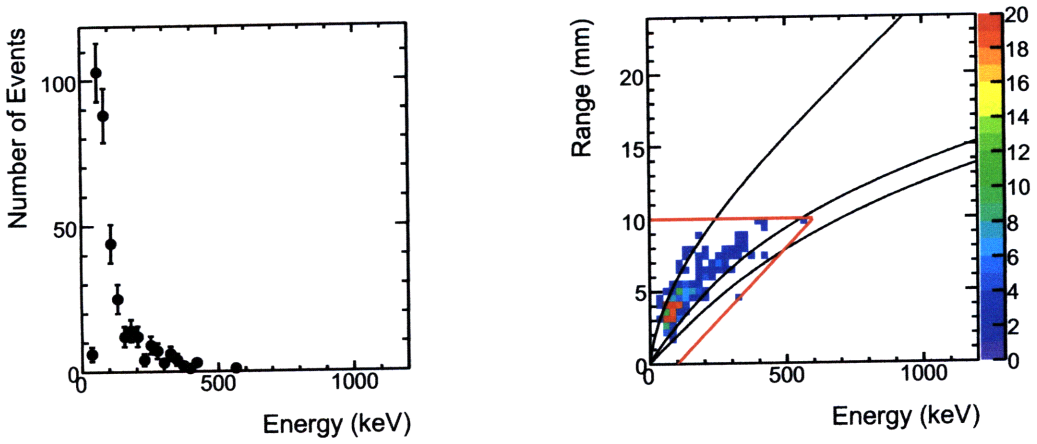

Figure 15: Energy (left) and range versus energy (right) distributions for the events in the ^{252}Cf data set which pass the cuts on sparks, multiple tracks, worms, edge crossing events, and range versus energy. Also shown are the SRIM predictions for alphas (top) and recoiling F (middle) and C nuclei (bottom). Shown in red is the location of the cut on range versus energy.

According to the SRIM predictions, a recoiling nucleus which travels 10 mm before depositing all of its energy corresponds to an nuclear recoil of approximately 700 keV for fluorine and 550 keV for carbon. These energies are well above the predicted distribution of WIMP induced nuclear recoils (see Figure 1), so we apply a cut on the range of tracks by requiring that signal background candidates have a reconstructed projected range less than 10 mm. In addition, we do not expect events to lie at low range and high energies below the SRIM range versus energy lines, so we require that the range of tracks be greater than (0.02 mm/keV)*(energy in keV)-(2 mm). Lines corresponding to these cuts on the range versus energy distribution are shown in red in Figures 14- 16. This cut is referred to as 'RvE' in the following tables and figures. From Figure 14 it is clear that this cut eliminates high energy alpha particles, high energy nuclear recoils, and worm events which have not already been cut. The energy and range versus energy distribution for the neutron data after applying this cut is shown in Figure 15. Of the 415 events events remaining before the cut on range, 344 events pass this additional signal selection cut.

With these signal selection cuts, we expect the distribution in Figure 15 to be dominated by nuclear recoils from ^{252}Cf neutrons. To account for the expected energy

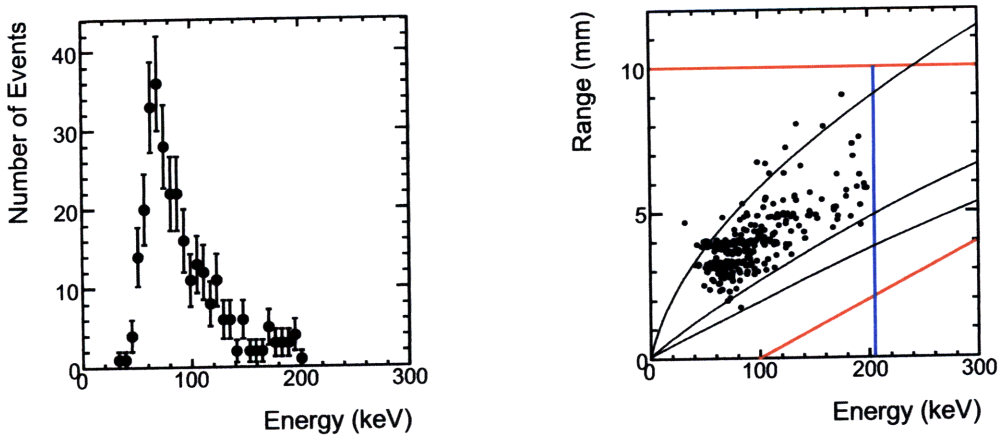

Figure 16: Energy (left) and range versus energy (right) distributions for the events in the ^{252}Cf data set which pass the cuts on sparks, multiple tracks, worms, edge crossing events, range versus energy, and energy. Also shown are the SRIM predictions for alphas (top) and recoiling F (middle) and C nuclei (bottom). Shown in red is the location of the cut on range versus energy, and shown in blue is the 200 keV cut on energy.

distribution of WIMP induced nuclear recoils (see Figure 1), we apply a final cut which requires signal candidates to have a reconstructed energy of less than 200 keV. This places a cut approximately 50 keV above the high energy tail of the expected energy distribution of WIMP induced nuclear recoils. The 297 events remaining after this energy cut in the ^{252}Cf data set are shown in Figure 16 with the location of the cut on reconstructed energy shown in blue. The lower left region containing the remaining events defines the region of background events. The applied cuts are summarized below, and Table 2 summarizes the effect of the cuts for the neutron data. From the energy distribution in Figure 16, we see that the absolute lower energy threshold for the track reconstruction and signal selection cuts is approximately 50 keV.

1. Spark Cut: number of pixels above threshold less than 55000
2. Tracks Cut: each event is in an image containing only one track
3. Worm Cut: tracks must not have energy density greater than 36.4 keV/mm and size less than 64 pixels
4. Edge Cut: all pixels in a track lie more than 2.29 cm from the edge of the image

5. Range Versus Energy (RvE) Cut: 10 mm < projected range < (0.02 mm/keV)*(energy in keV)-(2 mm)

6. Energy Cut: background candidates have reconstructed energy less than 200 keV

Cut	Events Cut	Events Remaining
No Cuts	0	11261
Spark	132	11129
Tracks	6093	5036
Worm	4348	688
Edge	273	425
RvE	71	344
Energy	47	297

Table 2: A summary of the cuts applied to the ^{252}Cf neutron data.

3.6 Signal Efficiency

To evaluate the efficiency of the track identification algorithms and signal selection cuts, a Monte Carlo study was done in which 2000 WIMP induced nuclear recoil events were simulated with a flat recoil energy distribution from 0-500 keV. The resulting simulated data was then analyzed with the analysis framework which was applied to the ^{252}Cf data set and the WIMP search data set. The left panel of Figure 17 shows the efficiency of the track identification as a function of energy in the region below the final energy cut of 200 keV. Above 175 keV, the efficiency of track identification is roughly 90%, but the efficiency then decreases to approximately 50% at 100 keV. At about 50 keV, the track identification efficiency is around 5%, and this is consistent with the absolute energy threshold of approximately 50 keV found in the application of the signal selection cuts to the ^{252}Cf neutron data.

The right panel of Figure 17 shows the efficiency of the signal selection cuts for the simulated Monte Carlo data as a function of simulated energy in the region below 200 keV. As can be seen from the figure, the cuts on sparks, number of tracks, and worms decrease the efficiency by only a few percent. However, the cut on edge crossing events decreases the efficiency to 46%. This large decrease in efficiency is due to the overly conservative restriction that all pixels in a track lie more than 2.29 cm from the edge

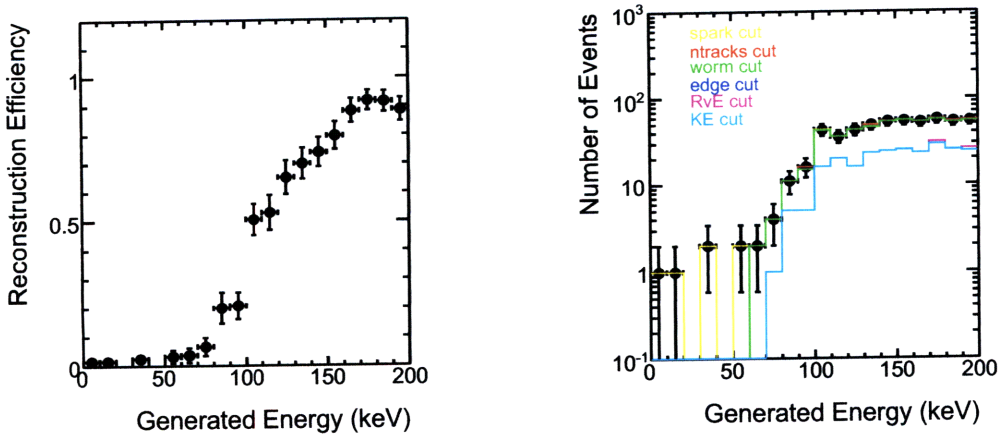

Figure 17: Left: the efficiency of the track identification as a function of energy from Monte Carlo studies. Right: the efficiency of the signal cuts as a function of energy from Monte Carlo studies.

of an image, and we believe that an improved efficiency can be achieved by relaxing this constraint. The subsequent cuts on reconstructed range and energy produce a negligible decrease in the overall efficiency. The efficiency of the signal selection cuts are summarized in Table 3.

Cut	Events Cut	Events Remaining	Efficiency
No Cuts	0	1187	1.000±0.000
Spark	0	1187	1.000±0.000
Tracks	8	1179	0.993±0.002
Worm	11	1168	0.984±0.004
Edge	617	551	0.464±0.021
RvE	0	551	0.464±0.021

Table 3: A summary of the signal efficiency for the cuts applied to the Monte Carlo WIMP induced nuclear recoil data.

4 Results

4.1 Application of Signal Selection Cuts to WIMP Search Data

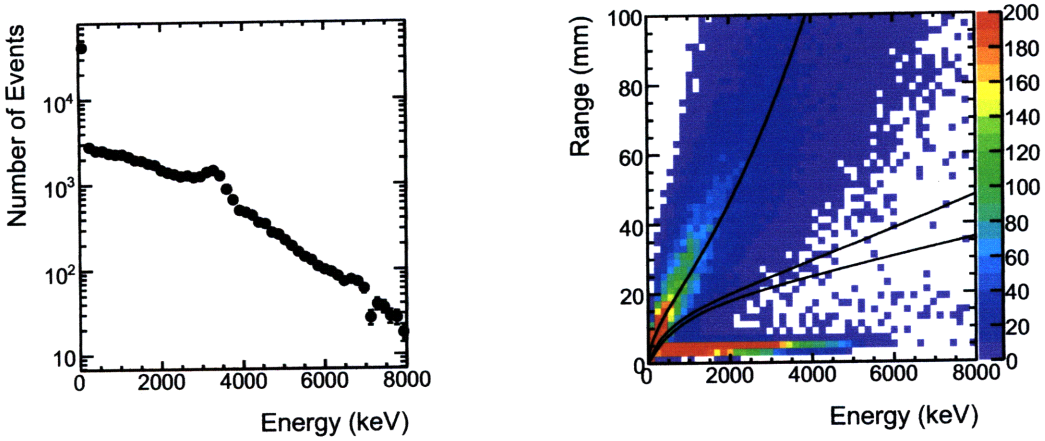

Figure 18: Energy (left) and range versus energy (right) distributions for the events in the WIMP search data set which pass the cuts on sparks and multiple track events. Also shown are the SRIM predictions for alphas (top) and recoiling F (middle) and C nuclei (bottom).

The total WIMP search data set consists of 458 runs each with 3000 one second exposures for a total exposure of 23.69 gram-days. Analyzing this data set as described in the previous sections, 224584 images were found to contain tracks which were above the threshold criteria. This corresponds to an overall rate of 163 mHz. The energy and range versus energy distributions for the reconstruction after applying the spark cut and requiring that each image contain only one track is shown in Figure 18. These preliminary cuts reduce the number of events to 85260. The range versus energy distribution displays two distinct populations. The broad band of events which are increasing in range roughly with the SRIM Monte Carlo predictions are alpha particle backgrounds and, at lower energy, possible nuclear recoil events. The population which increases in energy but is flat in range at about 5 mm are the worm events which arise due to interactions in the CCD. This population is in agreement with the population of worm events in the background data shown in Figure 11.

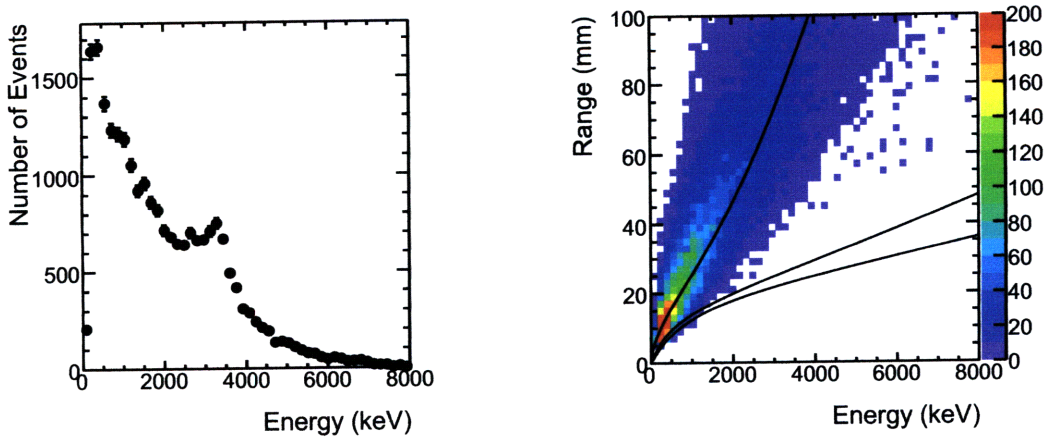

Figure 19: Energy (left) and range versus energy (right) distributions for the events in the WIMP search data set which pass the cuts on sparks, multiple tracks, and worm events. Also shown are the SRIM predictions for alphas (top) and recoiling F (middle) and C nuclei (bottom).

As was done with the neutron and Monte Carlo data, the cut on worm events in next applied. This reduces the number of events which pass the cuts to 23301, and the reconstructed distributions for these events are shown in Figure 19. The range versus energy distribution in the figure shows that the cut on worm events did in fact remove the band at constant range from the previous distribution. Now, the predominant population of background events are alpha particles which come from materials at the edges of the detector. These events do not lose their full energy in the view field of the detector, so their reconstructed energy is only the amount lost inside the view field. The energy and range versus energy of the data after making the cut on edge crossing events is shown in Figure 20. The remaining events are tracks that are fully contained in the camera view field, so their reconstructed energy it is the full energy of the alpha particle or recoiling nucleus. Examining the range versus energy distribution, the events above approximately 1 MeV appear to be consistent with the SRIM prediction for alpha particles. These events are expected to be the result of radon chain alpha decays from detector materials. This would result in several discrete peaks in the energy distribution in the range of 4-6 MeV. However, if the alpha particles are emerging from solid materials in the detector, they will lose substantial amounts of energy in passing through even microns of the material.

So, the smearing of the energy distribution to low energies (above 1 MeV where the distribution is dominated by alphas) is consistent with alpha decays occurring in detector materials.

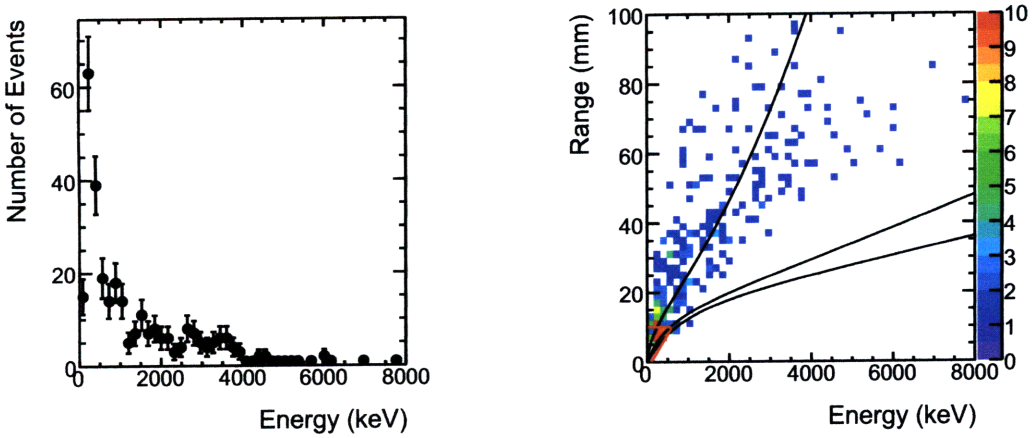

Figure 20: Energy (left) and range versus energy (right) distributions for the events in the WIMP search data set which pass the cuts on sparks, multiple tracks, worms, and edge crossing events. Also shown are the SRIM predictions for alphas (top) and recoiling F (middle) and C nuclei (bottom). Shown in red (lower left corner) is the location of the cut on range versus energy which will be applied.

Also shown in Figure 20 is the location of the cut on projected range. This cut eliminates the higher energy population of alpha particles, but it leaves the lower energy region in which the events cannot clearly be identified as either alphas or nuclear recoils by comparison to the SRIM predictions. After making the cut on the projected range versus energy, 56 events remain, and this corresponds to a rate of 40.8 μHz. The energy and range versus energy distributions for the events which pass this additional cut are shown in Figure 21. As the figure shows, these events go down in energy to about 125 keV, and they lie in the region where those events which are consistent with the alpha SRIM prediction cannot be clearly separated from those which are consistent with the nuclear recoil SRIM predictions.

Making the final cut, which requires that events have reconstructed energy less than 200 keV where WIMP induced nuclear recoils are expected, leaves 16 events that pass all of the required signal selection cuts. This brings the measured background rate to 11.6 μHz, a reduction of approximately 4 orders of magnitude from background

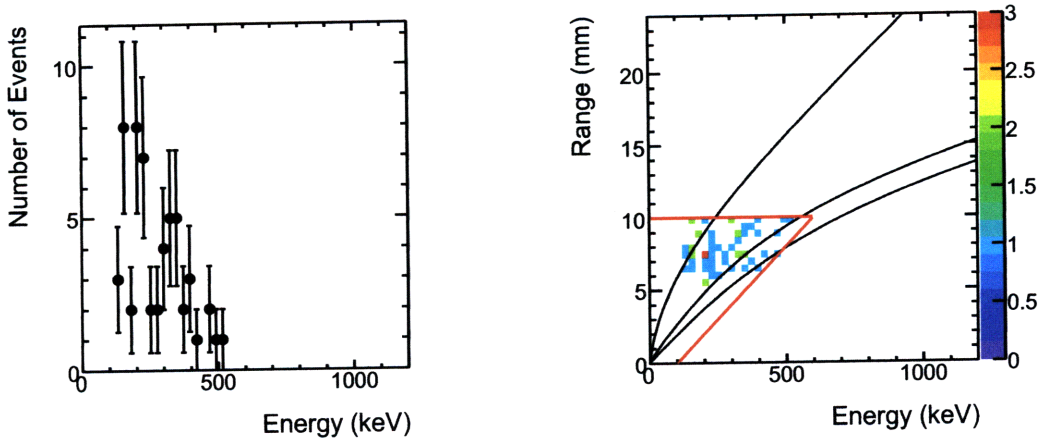

Figure 21: Energy (left) and range versus energy (right) distributions for the events in the WIMP search data set which pass the cuts on sparks, multiple tracks, worms, edge crossing events, and range versus energy. Also shown are the SRIM predictions for alphas (top) and recoiling F (middle) and C nuclei (bottom). Shown in red is the location of the cut on range versus energy.

rate before cuts. The remaining events are likely nuclear recoils from scattering of ambient neutrons in the detector gas.

4.2 WIMP Sensitivity

With these measurements of the signal efficiency (Figure 17) and number of background events (16), we now have the necessary components of Equation 1 to evaluate a limit on the WIMP induced nuclear recoil total cross section. We will only evaluate the limit for the spin-dependent case. The upper energy threshold has already been determined to be 200 keV based on the expected WIMP induced nuclear recoil energy distribution from Figure 1. As a simplification, we will not consider the energy dependence of the detector efficiency for this limit calculation. Examining the efficiency of track identification and of the signal selection cuts in Figure 17, the efficiency for both track identification and signal selection is above 0.46 for all energies in the range 100-200 keV. So, we can take the lower energy threshold to be 100 keV and the energy-independent efficiency to be 0.46. This does not exploit the higher efficiency at higher energies or the nonzero efficiency down to approximately 40 keV, however, more elaborate calculations than those done here are necessary to take advantage of

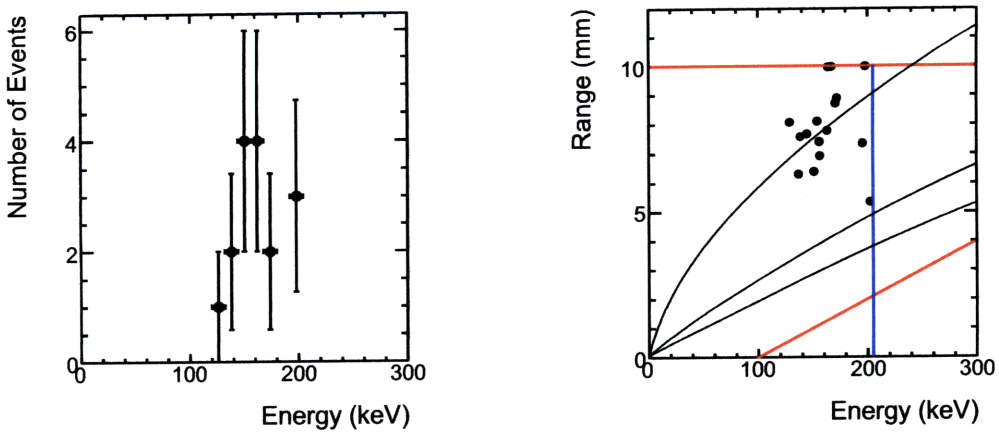

Figure 22: Energy (left) and range versus energy (right) distributions for the events in the WIMP search data set which pass the cuts on sparks, multiple tracks, worms, edge crossing events, range versus energy, and energy. Also shown are the SRIM predictions for alphas (top) and recoiling F (middle) and C nuclei (bottom). Shown in red is the location of the cut on range versus energy, and shown in blue is the 200 keV cut on energy.

the energy dependent detector efficiency. Therefore, this is a conservative estimate of the WIMP search sensitivity.

The ROOT implementation of the Feldman-Cousins method [30] is used to set the limit shown in Figure 23. The input parameters for this method are shown in Table 5, and they include the considerations described above, detector specifications, properties of the CF_4 target used in the experiment, and assumptions of the local WIMP distribution. The measured limit in Figure 23 reaches approximately a total WIMP-nucleus interaction cross section of approximately 5×10^{-34} cm^2. This shows a slight improvement over the NEWAGE measurement, but is roughly 4 orders of magnitude from the XENON10 limit [31] which is currently the leading SD WIMP limit. Although the limit set here is still orders of magnitude from the XENON10 limit, it is promising that the limit measured here comes from a running time and active mass which is approximately 2000 times less than that of the XENON10 experiment.

Cut	Rate of Events Failing Cut	Events Remaining	Rate of Remaining Events
No Cuts	0.00±0.00 Hz	224584	163±0.0 mHz
Spark	72.9±0.2 mHz	124469	10.5±0.3 mHz
Tracks	28.5±0.1 mHz	85260	62.1±0.2 mHz
Worm	45.1±0.2 mHz	23301	17.0±0.1 mHz
Edge	16.7±0.1 mHz	305	222±13 μHz
RvE	181±11 μHz	56	40.8±5.4 μHz
Energy	29.1±4.6 μHz	16	11.6±2.9 μHz

Table 4: A summary of the cuts of applied to the WIMP search data. All rates are relative to the 1.374×10^6 second total exposure.

5 Conclusions

The measurements discussed here have utilized a optical readout DMTPC prototype detector with active fiducial mass of 1.29 grams at 75 Torr of CF_4. A 23.69 gram-day exposure of WIMP search data on the surface of the earth was acquired and analyzed as a first test of the DMTPC detector sensitivity. Data was also acquired to study camera background artifacts resulting, and data was acquired with a high rate neutron source in order to define signal selection cuts for the nuclear recoil events in the WIMP data. A study of electron diffusion was also performed in an attempt to better understand the detector and to help resolve discrepancies between existing measurements. A Monte Carlo study of WIMP induced nuclear recoils under the experimental conditions was then performed in order to determine the efficiency of the detector and of the signal selection cuts. After applying the signal selection cuts to the 15.9 day live time exposure, 16 background events remained which gives a background rate of 11.6±2.9 μHz. This is a reduction in the total number of tracks found by over 4 orders of background, and this is an impressive demonstration of the background rejection capabilities of low-pressure time projection chambers in dark matter experiments. These measurements were then used to set the WIMP limit shown in Figure 23 which shows a slight improvement over the NEWAGE measurement, but is roughly 4 orders of magnitude from the XENON10 limit which is currently the leading SD WIMP limit. As previously described, the measured WIMP limit shown in Figure 23 does not fully exploit the detector's efficiency, at low energies. Rough calculations show that a possible improvement of an order of magnitude can be gained

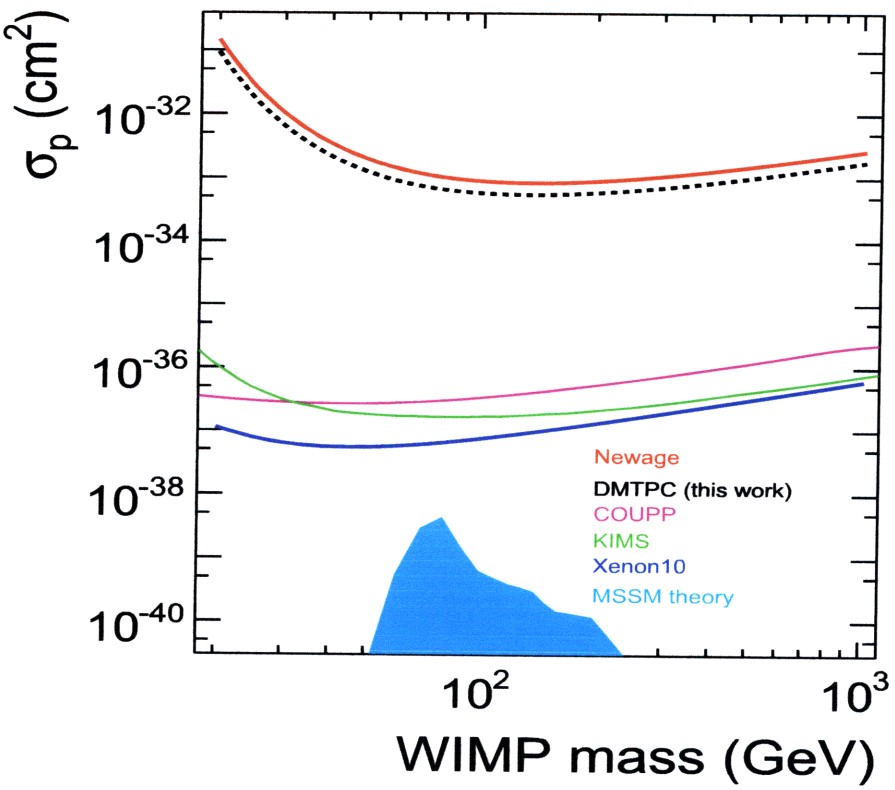

Figure 23: The WIMP limit at 90% confidence level measured by this experiment using the ROOT implementation of the Feldman-Cousins method compared with limits published by other experiments and a supersymmetric prediction for WIMP interaction cross sections.

by exploiting the energy dependence of the signal efficiency down to approximately 40 keV. Furthermore, reduction of the overly conservative cut on edge crossing events may improve the measurement by approximately a factor of two.

The measurements discussed here can be further improved in several ways. First, a detector built in a clean environment with radio-pure materials will reduce backgrounds caused by radiation sources in the detector material. A second way to reduce backgrounds is operation of the detector below the surface of the earth. This would reduce background from cosmic rays, and in particular the worm and neutron backgrounds which can mimic a WIMP signal at low energies. Additionally, improvements in detector design will allow for operation at higher anode and cathode voltages which

Input Parameter	Value
Target Mass Number	19
Spin Factor ($\lambda^2 J(J+1)$)	0.647
Fraction Usable SD	0.864
Active Mass	1.49 gm
Live Time	15.9 days
Detector Efficiency	0.46
Lower Energy Threshold	100 keV
Upper Energy Threshold	200 keV
Number of Background Events	16
Number of Unpaired Protons	1
Number of Unpaired Neutrons	0
Assumed Local WIMP Density	0.4 GeV/cm^3
Assumed Local WIMP Speed	230 km/s

Table 5: A summary of the input parameters for the ROOT implementation of Feldman-Cousins method which is used to set the WIMP limit shown in Figure 23.

will increase the gain of the detector. Recent improvements to the detector described here have resulted in gains approximately 5 times higher than the gain for the operating conditions of the data taken for these measurements. With a higher gain, the signal efficiency at low energies is improved, and the resulting lower threshold in energy will result in better sensitivity. Another potential improvement is the use of the direction of reconstructed tracks to make a cut on events which are directionally inconsistent with the expected dark matter wind. This requires a reconstruction of the 3-dimensional angle of tracks which was not possible with the data taken for the measurements presented here. Using the timing profile of a signal from PMTs or the charge deposited on the anode, it may be possible to estimate the angle out of the image plane for tracks. This, together with the reconstructed angle in the image plane, may give the necessary 3-dimensional angular resolution to implement directional detection. Finally, the measurements can be vastly improved by detectors which utilize a much larger fiducial volume and much longer exposure. Improvements are currently being made in all of these areas [ ].

6 Acknowledgements

This work has been done on behalf of the DMTPC collaboration [J. Battat, D. Dujmic, P. Fisher, S. Henderson, R. Lanza, A. Lee, J. Lopez, A. Kaboth, G. Kohse, J. Monroe, T. Sahin, G. Sciolla, R. Yamamoto, H. Yegoryan, Z. Zhou (Massachusetts Institute of Technology); S. Ahlen, K. Otis, H. Tomita (Boston University); A. Dushkin, H. Wellenstein (Brandeis University)], and the author acknowledges and thanks each member of the collaboration for his/her contributions to the work done here.

In particular, the author would like to thank Denis Dujmic for his extensive and invaluable help with the detector and analysis. The author also thanks Jocelyn Monroe and Peter Fisher for their constant help and support in this work. For their contributions to the analysis framework and Monte Carlo studies, the author also thanks Asher Kaboth, Jeremy Lopez, and Z. J. Zhou. Without the help from these individuals, this work would not have been possible.

References

[1] F. Zwicky, *The Astrophysical Journal* Vol. 86, 217 (1937).

[2] M. S. Roberts and A. H. Rots, *Astronomy and Astrophysics* Vol. 26, 483 (1973).

[3] J. P. Ostriker, P. J. E. Peebles, and A. Yahil, *Nature* Vol. 250, 309 (1974).

[4] V. C. Rubin, N. Thonnard, and W. K. Ford Jr., *The Astrophysical Journal* Vol. 225, L107 (1978).

[5] A. Refregier, *Annual Review of Astronomy and Astrophysics* Vol. 41, 645 (2003).

[6] C. H. Lineweaver and D. Barbosa, arXiv:astro-ph/9612146v2 (1997).

[7] D. Hooper and S. Profumo, *Physics Reports* Vol. 453, 29 (2007).

[8] M. S. Turner, *Physics Reports* Vol. 197, 67 (1990).

[9] G. G. Raffelt, *Physics Reports* Vol. 198, 1 (1990).

[10] L. J. Rosenberg and K. A. van Bibber, *Physics Reports* Vol. 325, 1 (2000).

[11] C. Boehm, P. Fayet, and R. Schaeffer, *Physical Review B* Vol. 518, 8 (2001).

[12] C. Savage et al., arXiv:0808.3607v3 [astro-ph] (2009).

[13] U. Chattopadhyay and D. P. Roy, *Physical Reveiw D* Vol. 68, 033010 (2003).

[14] J. R. Ellis, A. Ferstl and K. A. Olive, *Physical Review D* Vol. 63, 065016 (2001).

[15] G. D. Martinez et al., arXiv:0902.4715v2 [astro-ph] (2009).

[16] D. N. Spergel, *Physical Review D* Vol. 37, 1353 (1988).

[17] A. Green and B. Morgan, *Astroparticle Physics* Vol. 27, 142 (2007).

[18] M. S. Alenazi and P. Gondolo, *Physical Review D* Vol. 77, 043532 (2008).

[19] B. Morgan, A. M. Green and N. J. C. Spooner, *Physical Review D* Vol. 71, 103507 (2005).

[20] A. Pansky et al., *Nuclear Instruments and Methods in Physics Research A* Vol. 354, 262 (1995).

[21] L. G. Christophorou, et. al., *Journal of Physical and Chemical Reference Data* Vol. 25, 1341 (1996).

[22] A. Kaboth et al., [DMTPC Collaboration], *Nuclear Instruments and Methods in Physics Research A* Vol. 592, 63 (2008).

[23] B. Schmidt and S. Polenz, *Nuclear Instruments and Methods in Physics Researh A* Vol. 273, 488 (1988).

[24] M. G. Curtis, I. C. Walker, and K. J. Mathieson, *Journal of Physics D*, Vol. 21, 1271-1274 (1988).

[25] C. S. Lakshminarasimha, J. Lucas, and D. A. Price, *Proceedings of Industrial Electronic Engineers*, Vol. 120, 9 (1973).

[26] S. R. Hunter, J. G. Carter, and L. G. Christophorou, *Journal of Chemical Physics* Vol. 86, 693 (1987).

[27] P. G. Datskos, J. G. Carter, and L. G. Christophorou, *Journal of Applied Physics* Vol. 71, 15 (1992).

[28] D. Dujmic et al., [DMTPC Collaboration], "Transport Properties of Electrons in CF_4," (in preparation for publication to arXiv).

[29] M. J. Rivard and R. G. Zamenhof, *Journal of Applied Radiation and Isotopes* Vol. 61, 5 (2004).

[30] G. J. Feldman and R. D. Cousins, *Physical Review D* Vol. 57, 7 (1998).

[31] J. Angle et al., [XENON10 Collaboration], *Physical Review Letters* Vol. 101, 091301 (2008).

[32] G. Sciolla et al. [DMTPC Collaboration] arXiv:0903.3895 [astro-ph] (2009).